Supporting Information

On the Fate of Low-Lying Charge-Transfer Excited States in a Donor:Acceptor Blend with Large Energy Offset

Giacomo Londi[1], Saeed-Uz-Zaman Khan[2], Luca Muccioli[3], Gabriele D'Avino[4], Barry P. Rand[2,5] and David Beljonne[1]*

[1]Laboratory for Chemistry of Novel Materials, University of Mons, Place du Parc 20, 7000 Mons, Belgium

[2]Department of Electrical Engineering, Princeton University, Princeton, New Jersey 08544, United States

[3]Department of Industrial Chemistry, University of Bologna, Viale Risorgimento 4, 40136 Bologna, Italy

[4]Grenoble Alpes University, CNRS, Grenoble INP, Institut Néel, 25 rue des Martyrs, 38042 Grenoble, France

[5]Andlinger Center for Energy and the Environment, Princeton University, Princeton, New Jersey 08544, United States

*email: David.BELJONNE@umons.ac.be

Molecular Dynamics simulations

The three systems were modelled with a previously developed united atom force field for organic light-emitting diode (OLED) materials[1]. Charges of the united atoms were obtained by fitting the electrostatic potential (ESP charges) calculated at the optimized PBE0/def2-TZVP geometry. Concerning the validation of the force field (FF), in Ref.[1], where the FF parameters were optimized for reproducing the experimental crystal cells and densities of several polyaromatic compounds, NPB was taken as a test molecule outside the training set, giving an overall error of 1.1%. For HAT-CN, we obtained a lower but reasonable agreement, by means of NVT and NPT simulations at fixed cell angles using the same equilibration protocol discussed in Ref.[1], between the calculated cell dimensions a=b=23.464 Å, c=15.75 Å, and the experimental ones[2] a=b=23.637 Å, c=14.83 Å.

A horizontal graphene surface of 76.136 Å × 76.572 Å was chosen as a simple rigid and chemically compatible support and kept fixed during all the simulations. The vertical side of the simulation box was set to 400 Å to leave ample space for deposited molecules and avoid interactions between the two sides of the graphene + blend slab, since 3D periodic boundary conditions were used. Parameters for graphene-molecule interactions were obtained using Steele's potential[3] and Lorentz-Berthelot mixing rules. Deposition proceeded by randomly selecting the chemical species of the new molecule to be added at each step according to the desired molar fraction. Every new molecule was placed at about 20 Å above the forming organic layer, endowed with a velocity of 1 Å ps^{-1} directed parallelly to the normal to the graphene surface, and the dynamic of the system evolved for 100 ps at 500 K. At the end of this deposition step, if the last deposited molecule had desorbed, the step was repeated without randomizing again the molecular species, otherwise a further molecule was inserted following the same scheme. As a consequence of the randomness of the deposition, the final compositions do not match exactly the mol:mol ratio given in input (NPB:HAT-CN = 1:3, 9:1, 29:1). The actual compositions were of 239 NPB and 761 HAT-CN for the 1:3 sample (with HAT-CN molar fraction of 76.1 %, or 67.5% in weight), 897 and 103 for the 9:1 sample (10.3%, 7% in weight), and 1145 and 55 for the 29:1 sample (4.6%, 3% in weight). The three systems were subsequently cooled and equilibrated at 300 K, and subsequently at 200 K and 100 K. At each temperature, equilibration was continued until no appreciable drift of the total energy was detected, compared to its thermal fluctuations: e.g. at 100 K the energy fluctuations were of ca. 0.02 kcal mol^{-1}.

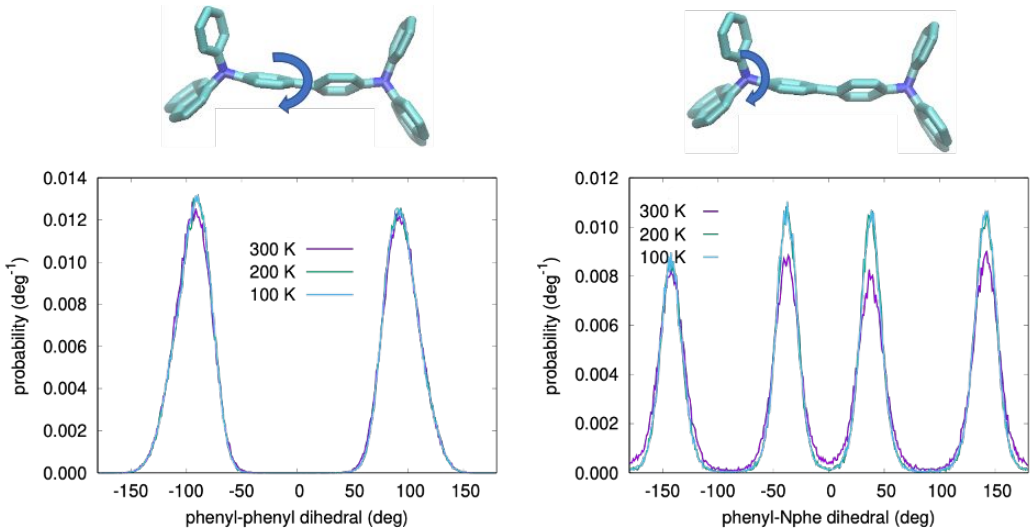

Figure S1: Distribution of the two main NPB dihedral angles for the sample at 4.6% HAT-CN molar fraction, as obtained from MD simulations at three different temperatures.

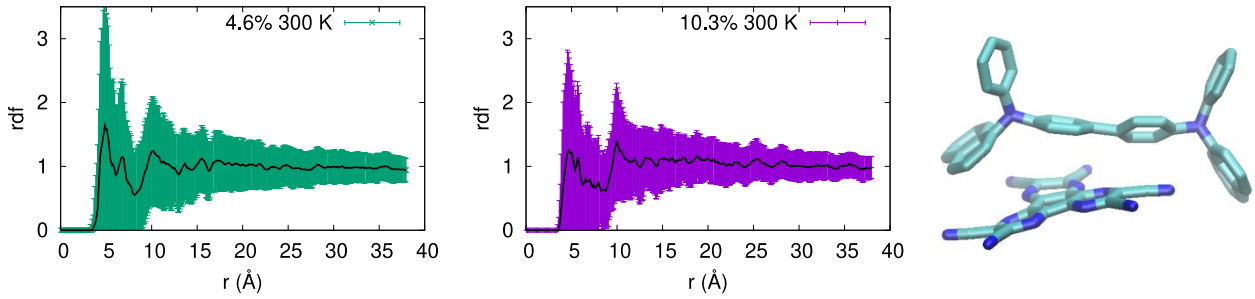

Figure S2: Radial distribution function of NPB:HAT-CN pairs at two different concentrations. A typical configuration corresponding to intermolecular distances of about 5 Å is shown on the right: the HAT-CN azatriphenylene core lies adjacent and parallel to the central biphenyl moiety of NPB.

Electronic structure calculations

The gas-phase energy of a generic electronic state, is calculated as:

$$\mathrm{E}(\mathbf{R}_{\mathrm{MD}}) = \mathrm{E}^{\mathrm{GW}}(\mathbf{R}_{\mathrm{X}}) + \left[\mathrm{E}^{\mathrm{DFT}}(\mathbf{R}_{\mathrm{MD}}) - \mathrm{E}^{\mathrm{DFT}}(\mathbf{R}_{\mathrm{X}})\right] \#(\mathrm{S1})$$

where $\mathbf{R}_{\mathrm{MD}}$ labels the geometry of a given molecule in the MD sample and $\mathbf{R}_{\mathrm{X}}$ is a reference geometry, taken from the bulk crystal structure of both species. In practive, the energy at the crystal geometry

was calculated with the *GW* method, which ensure accurate absolute values, and the energy deviations from it, as obtained from classical MD simulation geometries, were evaluated with DFT. Gas-phase *GW* calculations were performed with the FIESTA code, starting from DFT calculations, based on the PBE0 functional, obtained with the ORCA package.[4] A partial self-consistent scheme on the eigenvalues (ev*GW*) was exploited, along with Gaussians basis set of the Dunning's correlation-consistent family (cc-pVXZ, where X = 2, 3). Then, quasi-particle energy levels were extrapolated to the complete basis set limit.[5] The universal Weigend Coulomb fitting set of functions was used as auxiliary basis in the resolution of identity (RI-V) approach.

The effect of intramolecular structural relaxation upon charging was considered by calculating, separately for NPB and HAT-CN, the intramolecular reorganization energy λ^q, averaged on the charging and discharging processes:

$$\lambda^q = \frac{\left|E^q(\boldsymbol{R}_0) - E^q(\boldsymbol{R}_q)\right| + \left|E^0(\boldsymbol{R}_q) - E^0(\boldsymbol{R}_0)\right|}{2} \#(S2)$$

where q stands for the charge on the molecule and $\boldsymbol{R}_0$, $\boldsymbol{R}_q$ indicate the equilibrium geometries of neutral and charged states. Geometries were optimized at the DFT level (ωB97X-D/6-31G(d,p)), keeping the molecular soft degrees of freedom (dihedral angles) frozen, as to account only the contribution from high-frequency modes only[6,7]. This avoids double counting electron-vibration interactions, since the contribution of low-frequency vibrations was evaluated classically from MD simulations. With this caveat, the total internal reorganization energy for CT formation / recombination is $\lambda_{int} = \lambda_{NPB}^{+} + \lambda_{HAT-CN}^{-} = 262$ meV, with $\lambda_{NPB}^{+} = 184$ meV and $\lambda_{HAT-CN}^{-} = 78$ meV.

ME calculations[8,9] were parametrized with ESP atomic charges and polarizability tensor calculated with DFT at the ωB97X-D/6-311++G(d,p) level. ESP charges were computed for all molecules in one equilibrated MD configuration, in neutral, positively (for NPB) and negatively (HAT-CN) charged states. The polarizability tensor was calculated at neutral NPB and HAT-CN reference geometries, and the polarizability of charged species was set equal to that of neutral ones. Polarization energies for holes (Δ^+) and electrons (Δ^-) were calculated for spherical clusters of increasing radius centered at the molecule of interest, and then extrapolated to the bulk, infinite radius limit. The energy of CT states was calculated for molecular NPB:HAT-CN pairs in close contact, selected from MD samples by applying PBC in the XY plane and excluding molecules within 4 nm from the graphene substrate and vacuum interface in order to avoid empty spaces in the z direction.

The CT absorption band of a single NPB:HAT-CN dimer was calculated as a Frank-Condon progression:

$$Abs(E) = \vec{\mu}_{GS-CT}^2 \sum_{n=0}^{n_{max}} \frac{e^{-S} S^n}{n!} \delta\left(E - E_{CT}^{0,0} - n\hbar\omega_{eff}\right) \#(S3)$$

where δ is the Dirac delta function. The absorption spectrum of the blend was computed as the superposition of CT bands of NPB:HAT-CN dimers in the sample, summing up the intensity of the

individual vibronic transitions in bins of 100 meV. The CT band width was sourced from the energetic disorder of the sample and the convergence of the spectral shape was obtained with $n_{max} = 8$.

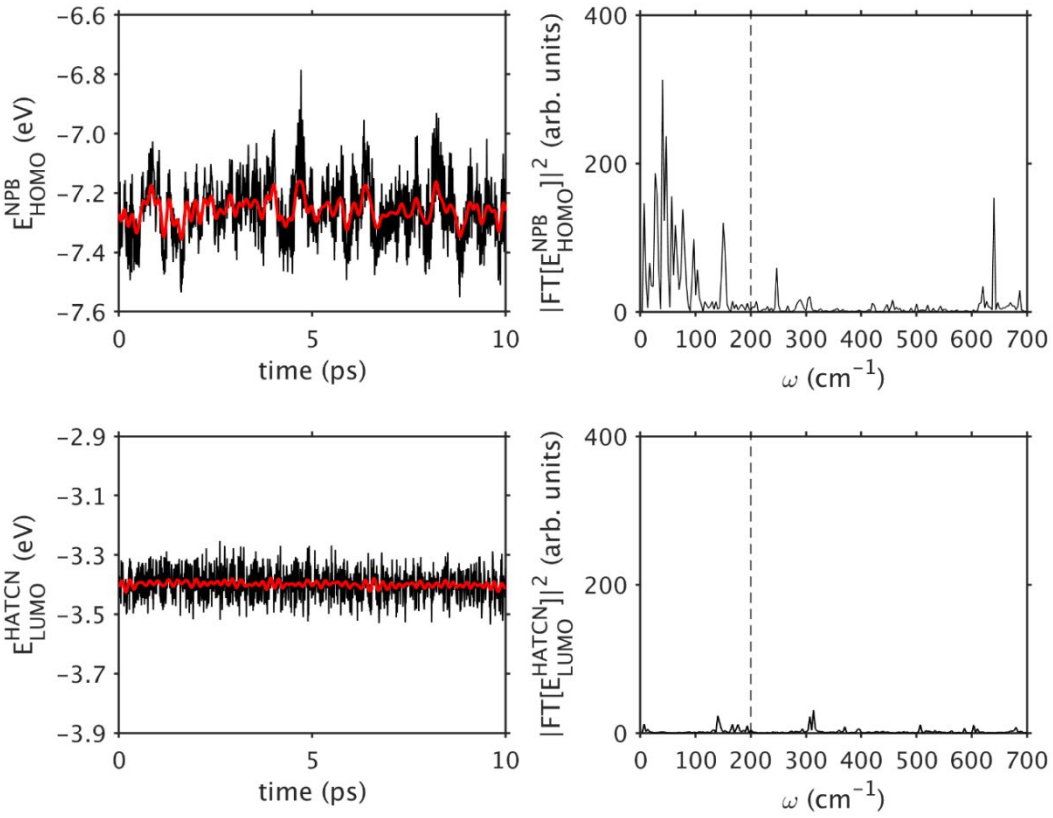

Figure S3: The conformational disorder was assessed with gas-phase DFT calculations performed at the MD geometries, quantifying the fluctuations of the NPB HOMO and the HAT-CN LUMO. The low- (high-)frequency disorder σ^x_{low} (σ^x_{high}) was evaluated as the standard deviation of the time series fluctuations (around the mean value of each molecule) after applying a low-pass (high-pass) filter to the original data (10 ps long trajectory sampled every 10 fs). The filter employed a rectangular function with energy cutoff equal to k_BT (~200 cm^{-1}). Left panels show the time series, as computed from MD geometries (black line) and after removing the high-frequency component (red line). Right panels show the power spectra of the unfiltered data, the vertical dashed line marks the 200 cm^{-1} cutoff frequency used to discriminate between low- and high-frequency components. These data refer to the 4.6% of HAT-CN sample at 300 K.

The calculation of IP_{NPB} and EA_{HAT-CN} (Figure 2 and Table 2 in the main text and TableS1 below) also provides a first validation of the methodology, since these values can be compared with experimental data measured on vapor deposited thin films of the two pure compounds: for NPB, IPs of 5.4-5.5 eV were measured by ultraviolet photoelectron spectroscopy (UPS)[10,11], while the EA of HAT-CN was reported to be larger than 4.9 eV as probed with low-energy inverse photoemission spectroscopy (LEIPS)[12], and estimated to be about 4.8 eV by comparison between UPS measurements on NPB:HAT-CN and NPB:F_4TCNQ films.[13] To further validate our results, it is also worth mentioning that UPS studies on mixed NPB:HAT-CN thin films indicate an increase of IP_{NPB} at increasing HAT-CN molar fraction.[11]

Table S1: Average energy of single carrier transport levels (in eV) and standard deviations σ_{tot}^{x} (in meV, where x stands for IP or EA). Energy fluctuations (in meV) were also quantified according to their nature: intramolecular σ_{conf}^{x}, intermolecular σ_{env}^{x}, static σ_{stat}^{x} and low-frequency dynamic disorder σ_{low}^{x}.

% HAT-CN	IP_{NPB}	σ_{tot}^{IP}	σ_{conf}^{IP}	σ_{env}^{IP}	σ_{stat}^{IP}	σ_{low}^{IP}
4.6	5.98	227	173	154	219	59
10.3	5.99	222	172	156	213	64
76.1	6.82	342	180	285	335	68

% HAT-CN	EA_{HAT-CN}	σ_{tot}^{EA}	σ_{conf}^{EA}	σ_{env}^{EA}	σ_{stat}^{EA}	σ_{low}^{EA}
4.6	4.18	157	36	149	157	11
10.3	4.19	152	16	152	152	12
76.1	4.94	260	14	259	259	14

Table S2: Average photovoltaic gap (E_{GAP}), CT state (E_{CT}), exciton binding energies (E_B) (in eV) and standard deviations σ_{tot}^{x} (in meV, where x stands for GAP or CT) for NPB:HAT-CN pairs at 100 K as a function of HAT-CN molar fraction. Energy fluctuations (in meV) were also quantified according to their nature: intramolecular σ_{conf}^{x}, intermolecular σ_{env}^{x}, static σ_{stat}^{x} and low-frequency dynamic disorder σ_{low}^{x}. Environmental reorganization energies λ_{env} (in meV) were calculated as $\lambda_{env} = \frac{\sigma^{2x}_{low}}{2k_BT}$. Note that for E_{GAP} and E_{GAP} the intermolecular σ_{env}^{x} and low-frequency dynamic disorder σ_{low}^{x} coincide and thus are given just once.

% HAT-CN	E_{GAP}	σ_{tot}^{GAP}	σ_{conf}^{GAP}	σ_{env}^{GAP}	σ_{stat}^{GAP}	σ_{low}^{GAP}	λ_{env}
4.6	1.81	280	185	227	273	60	210
10.3	1.84	260	164	220	252	65	243
76.1	1.98	371	173	346	365	69	278

% HAT-CN	E_{CT}	σ_{tot}^{CT}	σ_{stat}^{CT}	E_B	σ_B
4.6	1.44	288	281	-0.37	117
10.3	1.48	267	259	-0.36	110
76.1	1.53	390	384	-0.45	129

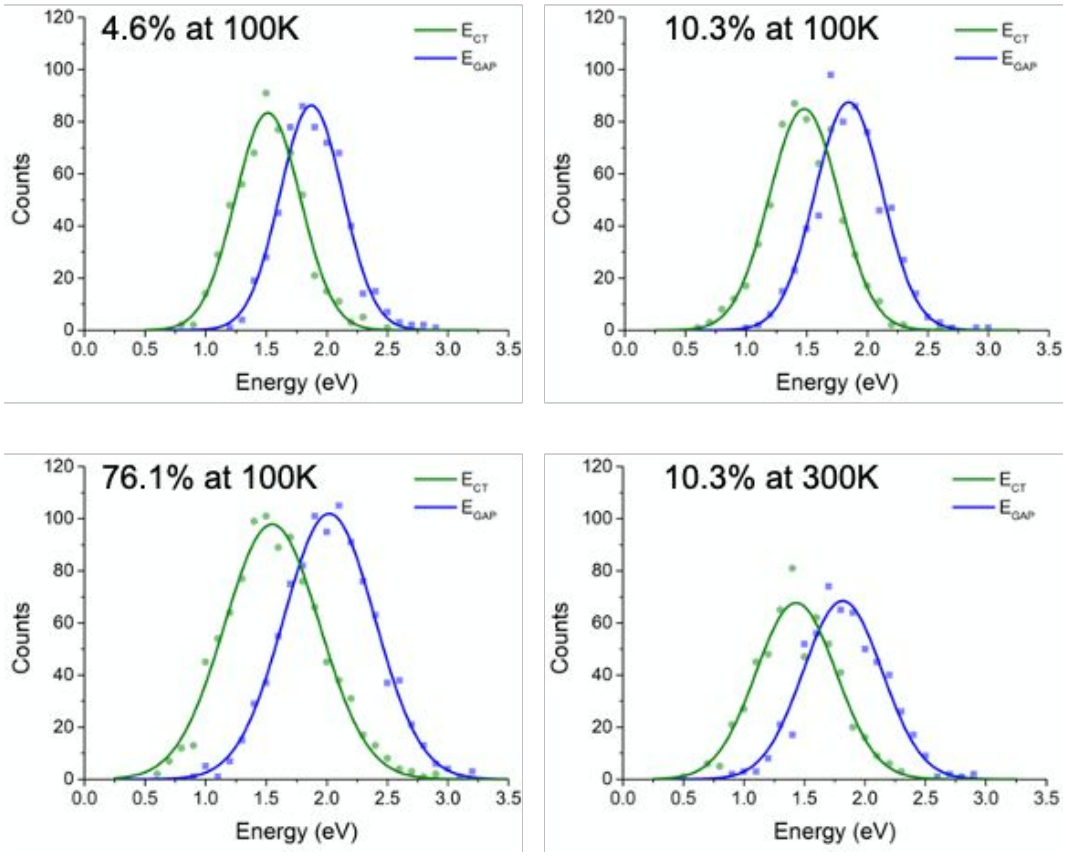

Figure S4: CT density of states (DOS) and distribution of gap energies at 4.6% and 76.1% HAT-CN molar fraction at 100 K (left) and at 10.3% HAT-CN molar fraction at 100 K and 300 K (right). Continuous lines are Gaussian fits.

The Generalized Mulliken-Hush (GMH) electronic couplings (entering equation 3 in the main text) were computed for NPB:HAT-CN dimers in the 4.6% and 76.1% of HAT-CN samples at 300 K at DFT/TD-DFT ωB97X-D/6-311G(d,p) level of theory, and using a polarized continuum model (PCM),[14] setting the scalar dielectric constant $\varepsilon = 3.0$ or $\varepsilon = 2.6$ for the sample at 4.6% or 76.1% of HAT-CN, respectively. The dielectric constant of the medium was obtained as the ratio between the unscreened interaction between an electron-hole pair (V_{eh}) and the corresponding screened exciton binding energy (E_B), both quantities accessible via ME calculations. The range-separation parameter ω[15] was set to 0.09 Bohr^{-1}, a value which ensures, at it should be, a strong intermolecular CT character of the first excited state in NPB:HAT-CN dimer calculations. The GMH electronic couplings (see Figures S5 and S6 below) were calculated as[16]:

$$J = \frac{\vec{\mu}_{GS-CT} E_{CT}^{0,0}}{\sqrt{\Delta\mu_{GS-CT}^2 + 4\vec{\mu}_{GS-CT}^2}} \quad \#(S3)$$

where $\vec{\mu}_{GS-CT}$ is the transition dipole moment, and $\Delta\mu_{GS-CT}$ the difference between the CT state permanent dipole moment and the ground state one.

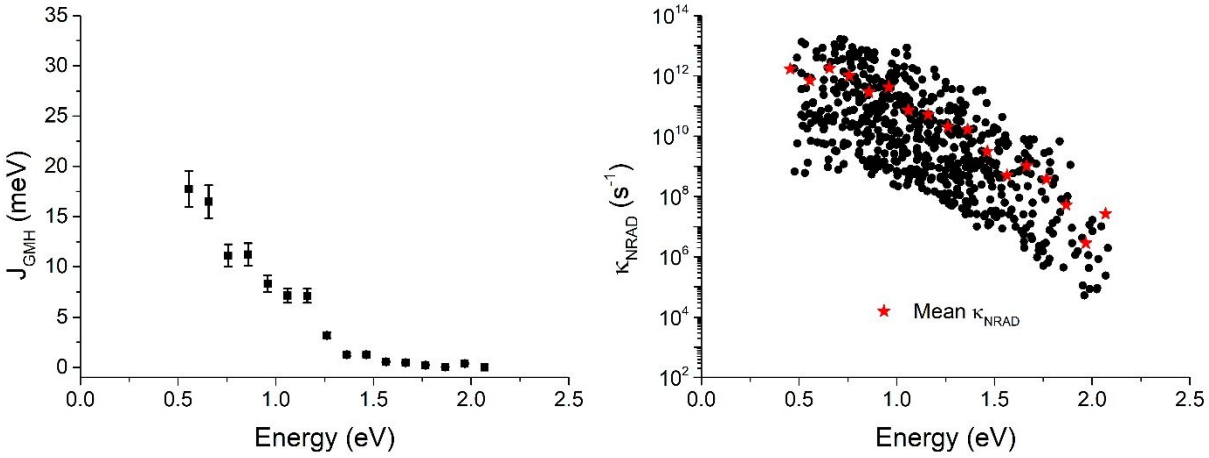

Figure S5: (left) Electronic coupling between the CT and the ground state computed with the Generalized Mulliken-Hush (GMH) scheme. Squares and error bars show mean values and standard deviations calculated over energy bins. (right) Non-radiative recombination rates for the select NPB-HAT-CN pairs in the sample (black dots) and their average over energy bins (red stars). Data calculated for the sample at 76.1% HAT-CN molar fraction at 300 K.

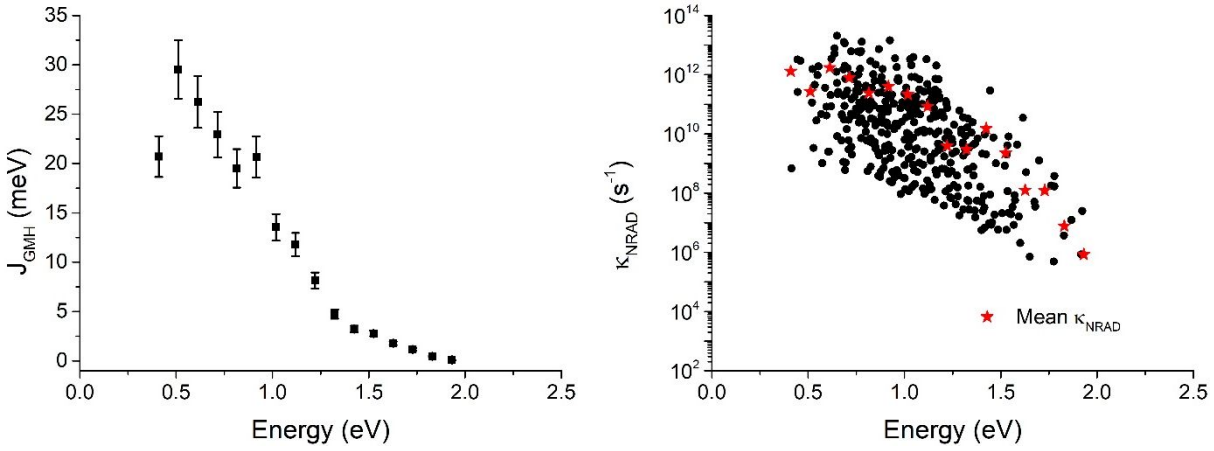

Figure S6: (left) Electronic coupling between the CT and the ground state computed with the Generalized Mulliken-Hush (GMH) scheme. Squares and error bars show mean values and standard deviations calculated over energy bins. (right) Non-radiative recombination rates for the select NPB-

HAT-CN pairs in the sample (black dots) and their average over energy bins (red stars). Data calculated for the sample at 4.6% HAT-CN molar fraction at 300 K.

EQE measurements

Samples for the EQE measurements were made on patterned ITO substrates (Colorado Concept Coatings). Substrates were cleaned by successive sonications in deionized water (15 min), acetone (10 min), and isopropanol (10 min) at 40 °C. Following the sonication step, the substrates were treated by oxygen plasma for 10 min.

Solar cell samples for the EQE measurements were made by thermally co-evaporating 100 nm of NPB (Nichem) and HAT-CN (Nichem) in a thermal evaporator (Angstrom Engineering Inc.), under ~10^{-7} torr base pressure, followed by 10 nm bathocuproine (BCP) (Lumtec) and 100 nm aluminum (Kurt J. Lesker Company) depositions. NPB and BCP were purified through thermal gradient sublimation, HAT-CN was used as purchased.

Temperature-dependent EQE spectra were measured by placing the sample inside a liquid N_2 based cryostat (Janis VNF-100). The temperature was controlled by a LakeShore 335 Cryogenic Temperature Controller. Monochromatic light was generated using Newport TLS-300X, which was chopped at 390 Hz with an optical chopper. The short-circuited device photocurrent was amplified by a current preamplifier (SR570, Stanford Research Systems) and detected by a lock-in amplifier (SR830, Stanford Research Systems). The incoming photon quantities from the monochromatic light source were estimated using calibrated Si and Ge photodiodes (Newport corporation). The cryostat was cooled down to 110 K first and then brought up to the room temperature while taking the measurements. Room temperature EQE spectra before and after cooling did not show any sign of device degradation due to the temperature change.

In the framework of Marcus theory of electron transfer, a Gaussian function fitted to the low-energy edge of the EQE spectrum is commonly used as an approximation to the lowest energy CT absorption line-shape[17], a technique that only considers vibronic broadening of the spectrum. However, Burke *et al.*[18] demonstrated that, when a Gaussian CT energetic distribution is assumed with a peak E_{CT} and standard distribution σ_{stat}, the overall CT absorption line-shape remains Gaussian with a shifted effective CT energy ($E_{CT(exp.)}$). The modified absorption line-shape also demonstrates an effective reorganization energy ($\lambda_{(exp.)}$). These effective CT spectral quantities are related to E_{CT} and reorganization energy (λ) of the electron transfer process as:

$$E_{CT(exp.)} = E_{CT} - \frac{\sigma_{stat}^2}{2k_BT} \qquad \text{(S5)} \qquad \lambda_{(exp.)} = \lambda + \frac{\sigma_{stat}^2}{2k_BT} \qquad \text{(S6)}$$

which can be extracted by fitting a Marcus type Gaussian line-shape to the low-energy EQE tail. The introduction of the static disorder in the CT absorption line-shape introduces a temperature dependence in the experimentally extracted CT state energy, which is clear from the $E_{CT(exp.)}$ and $\lambda_{(exp.)}$ values (see Figure S7a and S7b in SI) extracted from Figure 5a. A linear fitting to $E_{CT(exp.)}$ gives σ_{stat} of ~150 meV, responsible for the static broadening of the lowest energy CT EQE spectra. According to Burke *et al.*'s treatment of CT EQE spectra, the total variance of the CT EQE line-shape is:

$$\sigma_{EQE}^2 = \sigma_{stat}^2 + 2\lambda k_B T \#(S7)$$

where $\sigma_{dyn}^2 = 2\lambda k_B T$ is the contribution from the dynamic (vibrational) broadening of the CT spectra. The relative contribution of static disorder at a specific temperature could be defined as[19]:

$$D_{stat}(T) = \frac{\sigma_{stat}^2}{\sigma_{stat}^2 + 2\lambda k_B T} \#(S8)$$

The CT EQE lineshape, proposed by Burke *et al.*[18] considering a Gaussian energetic distribution of the CT states, is given as a function of incident photon energy (E):

$$EQE_{CT}(E) \propto \frac{1}{E\sqrt{2\pi(\sigma_{stat}^2 + 2\lambda k_B \mathrm{T})}} \exp\left(\frac{-(E_{CT} + \lambda - E)^2}{2\sigma_{stat}^2 + 4\lambda k_B T}\right) \#(S9)$$

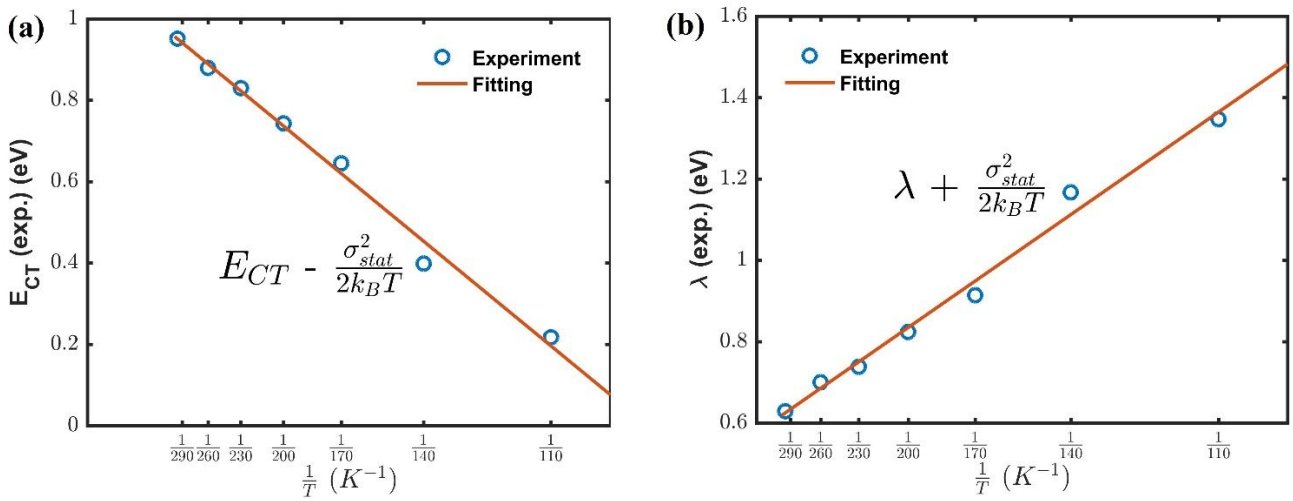

Figure S7: Effective (a) lowest CT state ($E_{CT(exp.)}$) and (b) reorganization ($\lambda_{(exp.)}$) energies extracted from Figure 5a. Fitting straight lines (in red) to the experimental data (blue circles) reveal peak of the CT energetic distribution (E_{CT}) at 1.40 eV and reorganization energy (λ) of 0.19 eV. The lowest

energy CT absorption peak ($E_{CT}+\lambda$) is at ~1.59 eV. The standard deviation of the CT energetic distribution (σ_{stat}) is 150 meV, from both (a) and (b).

Table S3: Static (σ_{stat}) and dynamic (σ_{dyn}) disorder contribution to the total CT EQE spectral broadening (σ_{tot}). Static disorder contribution to the total linewidth (D_{stat}) is dominant at all temperatures in a NPB:HAT-CN BHJ solar cell with 66.0% of HAT-CN.

Temperature, T (K)	σ_{stat} (meV)	$\sigma_{dyn}=\sqrt{2k_B\lambda T}$ (meV)	$\sigma_{tot}=\sqrt{{\sigma_{stat}}^2+{\sigma_{dyn}}^2}$ (meV)	$D_{stat}(T)=\frac{\sigma_{stat}^2}{\sigma_{tot}^2}$ (%)
110	150	60	162	85.73
140	150	67	164	83.66
170	150	74	167	80.68
200	150	80	170	77.85
230	150	86	173	75.18
260	150	92	176	72.64
296	150	98	179	70.22

References

(1) Moral, M.; Son, W.-J.; Sancho-García, J. C.; Olivier, Y.; Muccioli, L. Cost-Effective Force Field Tailored for Solid-Phase Simulations of OLED Materials. *J. Chem. Theory Comput.* **2015**, *11*, 3383–3392.

(2) Szalay, P. S.; Galán-Mascarós, J. R.; Clérac, R.; Dunbar, K. R. HAT(CN)6: A New Building Block for Molecule-Based Magnetic Materials. *Synth. Met.* **2001**, *122* (3), 535–542.

(3) Steele, W. A. The Interaction of Rare Gas Atoms with Graphitized Carbon Black. *J. Phys. Chem.* **1978**, *82* (7), 817–821.

(4) Neese, F. Software Update: The ORCA Program System, Version 4.0. *WIREs Comput. Mol. Sci.* **2018**, *8* (1).

(5) Li, J. *et al.* Host Dependence of the Electron Affinity of Molecular Dopants. *Mater. Horizons* **2019**, *6* (1), 107–114.

(6) Londi, G.; Dilmurat, R.; D'Avino, G.; Lemaur, V.; Olivier, Y.; Beljonne, D. Comprehensive

Modelling Study of Singlet Exciton Diffusion in Donor-Acceptor Dyads: When Small Changes in Chemical Structure Matter. *Phys. Chem. Chem. Phys.* **2019**, *21* (45), 25023–25034.

(7) Marqués, P. S. *et al.* Triphenylamine/Tetracyanobutadiene-Based π-Conjugated Push-Pull Molecules End-Capped with Arene Platforms: Synthesis, Photophysics, and Photovoltaic Response. *Chem. – A Eur. J.* **2020**, *n/a* (n/a).

(8) D'Avino, G.; Muccioli, L.; Zannoni, C.; Beljonne, D.; Soos, Z. G. Electronic Polarization in Organic Crystals: A Comparative Study of Induced Dipoles and Intramolecular Charge Redistribution Schemes. *J. Chem. Theory Comput.* **2014**, *10* (11), 4959–4971.

(9) D'Avino, G.; Muccioli, L.; Castet, F.; Poelking, C.; Andrienko, D.; Soos, Z. G.; Cornil, J.; Beljonne, D. Electrostatic Phenomena in Organic Semiconductors: Fundamentals and Implications for Photovoltaics. *J. Phys. Condens. Matter* **2016**, *28* (43).

(10) Hill, I. G.; Kahn, A. Organic Semiconductor Heterointerfaces Containing Bathocuproine. *J. Appl. Phys.* **1999**, *86* (8), 4515–4519.

(11) Amsalem, P.; Wilke, A.; Frisch, J.; Niederhausen, J.; Vollmer, A.; Rieger, R.; Müllen, K.; Rabe, J. P.; Koch, N. Interlayer Molecular Diffusion and Thermodynamic Equilibrium in Organic Heterostructures on a Metal Electrode. *J. Appl. Phys.* **2011**, *110* (11), 113709.

(12) Yoshida, H.; Yoshizaki, K. Electron Affinities of Organic Materials Used for Organic Light-Emitting Diodes: A Low-Energy Inverse Photoemission Study. *Org. Electron.* **2015**, *20*, 24–30.

(13) Falkenberg, C.; Olthof, S.; Rieger, R.; Baumgarten, M.; Muellen, K.; Leo, K.; Riede, M. The Role of Energy Level Matching in Organic Solar Cells- Hexaazatriphenylene Hexacarbonitrile as Transparent Electron Transport Material. *Sol. Energy Mater. Sol. Cells* **2011**, *95* (3), 927–932.

(14) Tomasi, J.; Mennucci, B.; Cammi, R. Quantum Mechanical Continuum Solvation Models. *Chem. Rev.* **2005**, *105* (8), 2999–3094.

(15) Brémond, É.; Pérez-Jiménez, Á. J.; Sancho-García, J. C.; Adamo, C. Range-Separated Hybrid Density Functionals Made Simple. *J. Chem. Phys.* **2019**, *150* (20), 201102.

(16) Cave, R. J.; Newton, M. D. Generalization of the Mulliken-Hush Treatment for the Calculation of Electron Transfer Matrix Elements. *Chem. Phys. Lett.* **1996**, *249* (1–2), 15–19.

(17) Vandewal, K.; Tvingstedt, K.; Gadisa, A.; Inganäs, O.; Manca, J. V. Relating the Open-Circuit Voltage to Interface Molecular Properties of Donor:Acceptor Bulk Heterojunction Solar Cells. *Phys. Rev. B* **2010**, *81* (12), 125204.

(18) Burke, T. M.; Sweetnam, S.; Vandewal, K.; McGehee, M. D. Beyond Langevin Recombination: How Equilibrium Between Free Carriers and Charge Transfer States Determines the Open-Circuit Voltage of Organic Solar Cells. *Adv. Energy Mater.* **2015**, *5* (11), 1500123.

(19) Linderl, T.; Zechel, T.; Hofmann, A.; Sato, T.; Shimizu, K.; Ishii, H.; Brütting, W. Crystalline versus Amorphous Donor-Acceptor Blends: Influence of Layer Morphology on the Charge-Transfer Density of States. *Phys. Rev. Appl.* **2020**, *13* (2), 24061.